Internal and Near Nozzle Measurements of Engine Combustion Network "Spray G" Gasoline Direct Injectors

Daniel J. Duke[a,b,*], Alan L. Kastengren[c], Katarzyna E. Matusik[a], Andrew B. Swantek[a], Christopher F. Powell[a], Raul Payri[d], Daniel Vaquerizo[d], Lama Itani[e], Gilles Bruneaux[e], Ronald O. Grover, Jr.[f], Scott Parrish[f], Lee Markle[g], David Schmidt[h], Julien Manin[i], Scott A. Skeen[i], Lyle M. Pickett[i]

[a]*Energy Systems Division, Argonne National Laboratory, Illinois, USA*
[b]*Laboratory for Turbulence Research in Aerospace & Combustion, Department of Mechanical & Aerospace Engineering, Monash University, Australia*
[c]*X-ray Science Division, Argonne National Laboratory, Illinois, USA*
[d]*CMT-Motores Térmicos, Universitat Politècnica de València, Valencia, Spain*
[e] *IFP Energies nouvelles, Rueil-Malmaison, France ; Institut Carnot IFPEN Transports Energie*
[f]*General Motors Research & Development*
[g]*Delphi Powertrain Systems*
[h]*Department of Mechanical & Industrial Engineering, University of Massachusetts-Amherst, Massachusetts, USA*
[i]*Sandia National Laboratories, Livermore, California, USA*

Abstract

Gasoline direct injection (GDI) sprays are complex multiphase flows. When compared to multi-hole diesel sprays, the plumes are closely spaced, and the sprays are more likely to interact. The effects of multi-jet interaction on entrainment and spray targeting can be influenced by small variations in the mass fluxes from the holes, which in turn depend on transients in the needle movement and small-scale details of the internal geometry. In this paper, we present a comprehensive overview of a multi-institutional effort to experimentally characterize the internal geometry and near-nozzle flow of the Engine Combustion Network (ECN) Spray G gasoline injector. In order to develop a complete picture of the near-nozzle flow, a standardized setup was shared between facilities. A wide range of techniques were employed, including both x-ray and visible-light diagnostics. The novel aspects of this work include both new experimental measurements, and a comparison of the results across different techniques and facilities. The breadth and depth of the data reveal phenomena which were not apparent from analysis of the individual data sets. We show that plume-to-plume variations in the mass fluxes from the holes can cause large-scale asymmetries in the entrainment field and spray structure. Both internal flow transients and small-scale geometric features can have an effect on the external flow. The sharp turning angle of the flow into the holes also causes an inward vectoring of the plumes relative to the hole drill angle, which increases with time due to entrainment of gas into a low-pressure region between the plumes. These factors increase the likelihood of spray collapse with longer injection durations.

1. Introduction

As emissions regulations continue to tighten and internal combustion technology continues to improve, better understanding of fuel injection is needed. Improving engine efficiency through the design of direct fuel injection systems has received a great deal of attention over the last 20 years, both in diesel and gasoline combustion [1].

The nozzle geometry and internal flow dynamics have a direct effect on spray atomization and entrainment [2]. This affects evaporation, mixing, and combustion [3]. Improvements which can be realized at the injection stage have the potential to contribute to emissions reductions [4] and increased efficiency. For example, recent measurements by Zhang et al. [5] have shown that gasoline injectors with laser-drilled and electro-discharge machined (EDM) holes can experience spray collapse at different conditions, and this has a measurable effect on soot emissions.

*Corresponding author
Email address: daniel.duke@monash.edu (Daniel J. Duke)

Duke, D.J., Kastengren, A.L., Matusik, K.E., Swantek, A.B., Powell, C.F., Payri, R., Vaquerizo, D., Itani, L., Bruneaux, G., Grover, R.O., Parrish, S., Markle, L., Schmidt, D., Manin, J., Skeen, S.A., Pickett, L.M., 2017. Internal and near nozzle measurements of Engine Combustion Network "Spray G" gasoline direct injectors. Exp. Therm. Fluid Sci. 88, 608–621. doi:10.1016/j.expthermflusci.2017.07.015

This paper focuses on the commonly-used multi-hole mini-sac type gasoline direct injector (GDI). GDI spray measurements are challenging for a variety of reasons. The plumes are closely spaced and have a tendency to merge or collapse [6–9]. It is difficult to optically access individual plumes. Strong entrainment effects and persistent unsteadiness in the spray after the needle reaches full lift limit the usefulness of steady-state analysis [10–13]. Flash-evaporation of the spray under low ambient pressure conditions is also possible when the ambient pressure is low and fuel temperature is high [14, 15].

GDI systems have been studied experimentally for over 25 years; much of the available data has been obtained from optically accessible engines or spray and combustion vessels [16, 17]. Intrusive techniques such as rate of injection (ROI), rate of momentum (ROM) and mechanical patternation are well established [18, 19]. A wide range of non-intrusive diagnostics have also been employed to study the spray and entrainment field. These include schlieren and shadowgraphy, Mie and Rayleigh scattering [17, 20–22], diffuse backlit illumination (DBI) [23–25], particle image velocimetry [12, 26, 27], laser absorption scattering [28], Raman spectroscopy [29] and laser induced fluorescence (LIF) [30–33] among others. Phase doppler interferometry (PDI) is also commonly used to measure droplet size and velocity where the flow is sufficiently dilute [21, 22, 34–39].

In addition to visible-light techniques, x-ray diagnostics have also been applied to GDI in recent years, using both bench-top [40–43] and synchrotron sources [44]. X-rays are able to penetrate dense sprays close to the nozzle where multiple scattering makes visible light imaging difficult [45]. High-energy x-rays can penetrate the metal of the nozzle to reveal the internal geometry [46]. The high flux from a synchrotron x-ray source enables single shot measurements with sub-microsecond time resolution [47]. Time-resolved radiography [44] provides quantitative measurements of liquid mass under non-evaporative conditions, and time-resolved tomography [48] provides quantitative planar density measurements through dense multi-jet sprays, revealing plume-plume interactions and shot-to-shot variations. Recently, Li et al. [49] have used ultra-fast auto-correlation x-ray phase contrast imaging to measure the velocity of liquid structures in the near-field of GDI sprays.

In order to obtain a complete picture of the internal and near nozzle flow of GDI nozzles, a multi-technique, multi-institutional approach is required, since no single technique can provide all the necessary data [17]. However, the multitude of boundary and initial conditions make it difficult to compare the findings of one study to another. The Engine Combustion Network (ECN) seeks to address the problem of facility limitations and variability through the specification of standard injectors and conditions [50]. Prior ECN work on diesel direct injection [45, 51] has now been extended to encompass GDI through the Spray G specification.

The ECN also provides a central experimental resource for model validation under well-defined conditions. Modeling forms a cruicial component of GDI research [52, 53]. A range of models for injector internal and near-nozzle flow continue to be developed, including volume-of-fluid methods [54, 55], mixed-fluid models [56, 57], and others. Recent simulations of Spray G suggest that complex transients in the vorticity of the sac flow play an important role in dictating the unsteadiness of the exit flow conditions and the mass balance between the plumes [58].

In this paper, we present a comprehensive overview of the internal and near-nozzle flow of the ECN Spray G injector. A wide range of techniques from multiple institutions have been used, including x-ray tomography, x-ray radiography, ROI, ROM, PDI, and LIF, among others. These new data build upon previously published work, including diffused backlit imaging (DBI), liquid and vapor penetration data from Manin et al. [24] and Payri et al. [9], Mie and Rayleigh scattering data from Blessinger et al [23], and ROI and ROM data presented by Payri et al. [19, 59]. Numerical simulations of the internal and near-nozzle flow are also used to explain trends in the experimental data, although a complete discussion of simulation efforts for Spray G is outside the scope of this paper. The focus is on internal and near-nozzle measurements under non-flashing conditions. The effects of flash-boiling and evaporation are topics of ongoing research [15] that will be covered in future work. The data presented in this paper are available as a reference for modelers, and can be shared upon request.

2. The Spray G injector

The ECN Spray G injector is a nominally axisymmetric eight-hole solenoid driven gasoline direct injector with a standard mini-sac form factor (see Fig. 1a-b). A set of 12 nominally identical injectors are available;

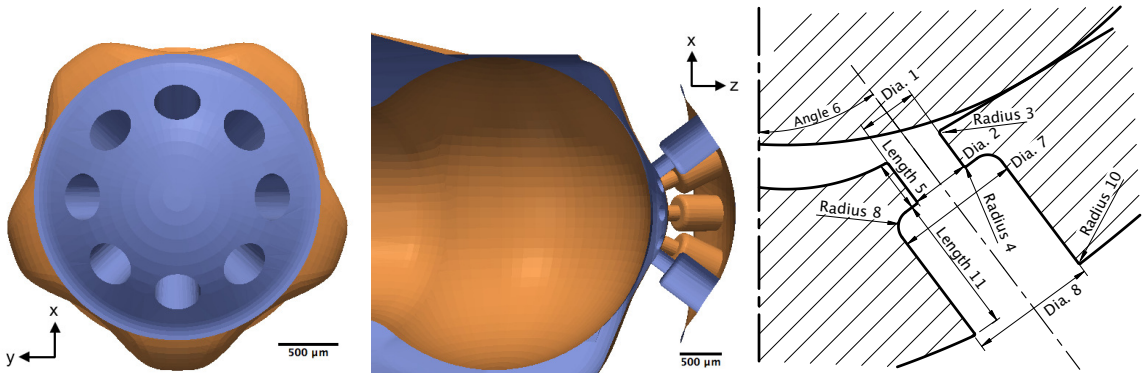

(a) Front view

(b) Side cut plane view

(c) Cut plane of hole, showing key dimensions. The numbers refer to the columns in Table 2.

Figure 1: Nominal (design) geometry of the Spray G injector.

Variable	**Spray G condition (nominal)**	**Argonne x-ray condition**
Fuel	*iso-octane*	*gasoline calibration fluid w/contrast agent*
- Temperature	363 K	298 K
- Injector body temp.	363 K	298 K
- Initial injection pressure	20 MPa	19 MPa
- Density	659 kg/m^3	838 kg/m^3
- Viscosity	0.3 cSt	1.15 cSt
- Vapor pressure	75 kPa	0.6 kPa
Ambient gas	N_2	N_2
- Temperature	573 K	298 K
- Pressure	5.97 bar	3.15 bar
- Density	3.5 kg/m^3	3.6 kg/m^3

Table 1: Nominal boundary conditions for Spray G, and conditions achieved during the x-ray experiments at Argonne.

these have been characterized using mechanical patternation, ROI, and backlit spray imaging following SAE J2715 protocol [60]. The six best-matched injectors were selected and circulated amongst participating institutions. Standard electronic driver boxes were supplied with each injector, in order to standardize the command signal delivered to the solenoid. This ensures a matched ramp rate and needle lift profile. A short injection duration of 680 µs was specified. In order to investigate persistent unsteady spray behavior, longer injections of 2 to 3 ms were also investigated.

The Spray G experimental standard was defined for these injectors using iso-octane at 363K / 90°C and 20 MPa, as per Table 1. Evaporative, non-combusting conditions were desired, so an ambient N_2 environment at 573K / 300°C and 6 bar was specified as the Spray G standard. The x-ray experiments conducted at the Advanced Photon Source (APS) at Argonne National Laboratory were restricted to non-evaporative conditions at room temperature for both the ambient gas and fuel. The chamber pressure was lowered to 3.15 bar, to match ambient density. A low-volatility gasoline surrogate (Viscor 16br, Rock Valley Oil & Chemical Company) with a cerium contrast agent (Rhodia DPX9, 9:1 v/v, 4.4% Ce by weight) was used. The fuel properties and conditions for the Argonne experiments are also shown in the right-hand column of Table 1. All other experiments presented in this paper conform to the nominal Spray G conditions.

3. Geometric characterization

3.1. Static x-ray tomography

The internal geometry of Spray G injector AV67-028 was characterized using high-resolution x-ray tomography at the 7-BM beamline of the APS at Argonne [61]. A schematic of the facility is shown in Figure

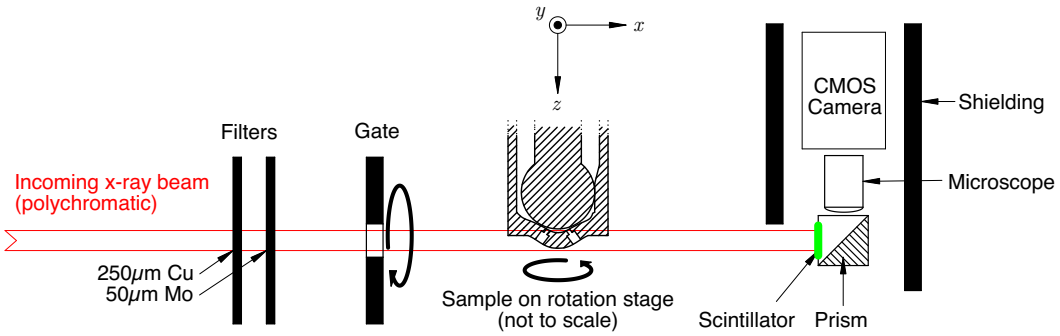

Figure 2: X-ray tomography setup at Argonne.

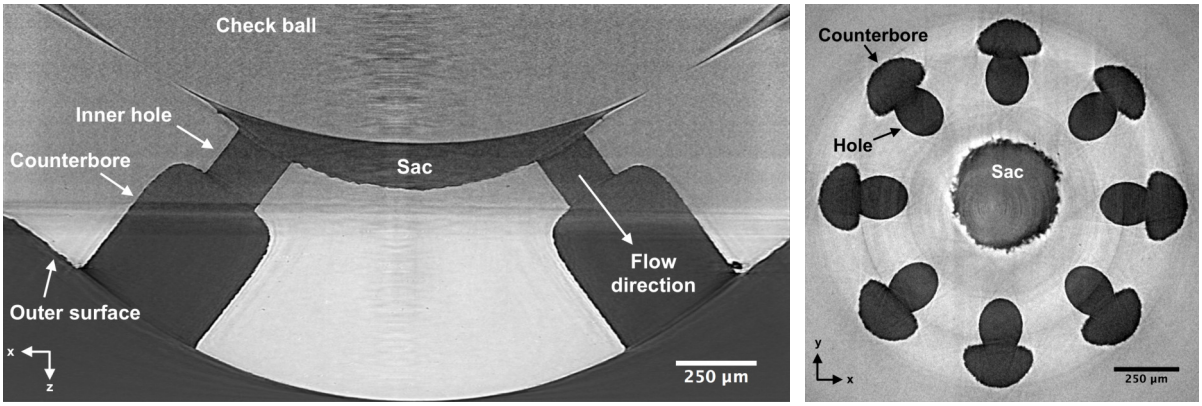

(a) Saggital plane.

(b) Transverse plane at $z = 0.63$ mm from injector tip.

Figure 3: Sample x-ray tomography images of Spray G Injector #28 from Argonne.

2. The injector was imaged with a spatial resolution of 1.17 μm per pixel and the three-dimensional geometry reconstructed using TomoPy, an open-source Python toolkit developed at Argonne [62]. Since the spectrum of the beam was known and the sample composition was relatively homogeneous, beam hardening artifacts were removed from the reconstructions through a lookup table, which converted the measured intensity to an equivalent path length of iron [63].

Sample cut-planes through features of interest in the Spray G injector are shown in Figure 3. Eleven key dimensions were identified which were deemed most critical to correctly modeling the flow inside and near to the nozzle, as per Figure 1c. These include the hole drill angle, inner hole length and diameters at each end, the counterbore length and diameters at each end, the corner radii at the inlet to the inner hole and the counterbore fillet radius. Measurements of these parameters are shown in Table 2. The lengths and diameters were computed by fitting elliptical profiles to the reconstructed intensity data along each hole, without isosurfacing, smoothing or interpolation. The major and minor diameters were averaged over several hundred measurement locations, as the holes were circular (no ellipticity, since the difference between major and minor diameters was less than the spatial resolution). The corner radii were measured at 360 positions around each hole and azimuthally averaged. The local hole inlet radii varied from 3 μm up to 20 μm, with the larger radii measured at the upper side of the hole, following the direction of flow.

The most important variations between the holes were the inlet diameter and length. The spread between minimum and maximum inlet diameter was 2% of the mean, which equates to a 4% spread in hole cross-section area. Table 2 shows that all hole diameters are 7-12% greater than the design dimension. These values were in good agreement with optical microscopy measurements [24]. The inner hole taper was very small, below the spatial resolution limit of the measurements. The length of the holes varied by 22%, leading to a wide range of L/D ratios from 0.8 to 1.0. These small-scale variations between the holes are not captured by the nominal geometry (Figs. 1a-b); this will affect the accuracy of simulation results and generate variations

	X-ray tomography measurement								Uncert-	Design
Hole Number	**1**	**2**	**3**	**4**	**5**	**6**	**7**	**8**	**ainty**	
1 - Hole inlet dia. (μm)	175	173	173	173	172	172	171	171	1.8	165
2 - Hole outlet dia. (μm)	175	175	173	173	173	172	172	172	1.8	165
3 - Hole inlet radius (μm)	4	4	4	3	5	4	5	5	1.8	0
4 - Hole outlet radius (μm)	7	7	6	6	7	7	7	7	1.8	0
5 - Hole length (μm)	154	172	168	161	143	139	139	139	1.8	170
6 - Drill angle (degrees)	36.1	37.0	37.9	37.9	38.1	37.2	36.7	36.3	0.2°	37
7 - C'bore inlet dia. (μm)	380	380	381	386	384	384	383	383	1.8	388
8 - C'bore outlet dia. (μm)	395	393	394	393	394	393	395	395	1.8	388
9 - C'bore fillet (μm)	52	54	46	56	38	42	55	55	1.8	40
10 - C'bore exit radius (μm)	9	9	8	8	9	9	9	7	1.8	0
11 - C'bore depth (μm)	397	398	397	396	396	386	391	396	1.8	470
Actual/design area ratio	1.12	1.10	1.09	1.10	1.08	1.08	1.08	1.07	0.01	
Inner hole L/D ratio	0.88	0.99	0.97	0.93	0.83	0.81	0.81	0.81	0.01	1.0

Table 2: Critical geometric features of each hole of the Spray G # 28 injector, measured from x-ray tomography and compared to design dimensions.

from hole to hole.

To further investigate the metrology of the nozzle interior, the tomography data were post-filtered using a Chambolle algorithm [64] and isosurfaced using the 'Seg3D' software package [65]. The surface is shown in Figure 4(a,c). The indicated co-ordinate system follows the SAE J2715 convention [60] with +z being the axial distance from the injector tip. The reconstruction clearly shows an uneven surface finish, which matches optical microscopic metrology of the nozzle surface and hole region performed at Sandia (Figure 4b). This rough surface finish was found to include many of the interior surfaces, including the counterbores and nozzle holes [66], which were manufactured by EDM. The size of the surface features is on the order of 6 to 8 μm.

Defects on the order of 10 μm were also found inside several of the nozzle holes; see Figure 5. These defects are relatively large (5-6% of the hole diameter) and are located near the sharp inlet edges to the holes where cavitation and/or flow separation is expected [14, 67]. Both the surface roughness and these hole-inlet defects are expected to have a significant effect on the internal flow [66], yet these have not been accounted for in numerical simulations. Isosurfaces which include these defects are available to modelers on request. This geometry has a higher resolution (by a factor of 4.3) and higher SNR than the previously published commercial CT data for these injectors [24]. A more detailed comparison of the various methods of characterizing injector geometries is a matter of ongoing research.

3.2. Hydraulic and mechanical charaterization

The dynamics of the needle motion in Spray G injectors were measured under non-evaporative conditions using time-resolved x-ray phase contrast imaging at the APS 32-ID beamline at Argonne [68]. A detailed explanation of the setup and methodology can be found in prior work [46, 51, 69]. In brief, the injector was mounted in a pressurized spray chamber at the Argonne conditions listed in Table 1. A polychromatic x-ray beam was used to image the internal components of the injector at 120 kHz with a pixel resolution of 1.9 μm. The motion of the needle was measured for 30 injections each at two locations and from three rotation angles of the injector body. Using image cross correlation and triangulation, the mean and standard deviation of the three-dimensional translation of the needle was computed for several injection durations. The needle consists of a check ball which acts as the valve (see Fig. 3a) which is attached to a stem that passes through the upper flow passage to attach to the spring and solenoid assembly. For clarity, we refer to the entire check ball and stem assembly as the needle.

The data were compared to rate-of-injection (ROI) data, in order to understand how deviations in needle motion relate to flow rate transients. Measurements supplied by CMT and GM R&D were performed using standard long tube type rate meters (piezoelectric pressure measurement type). The total injection rate from all the holes (mg/ms) was measured against injection pressure over time. There were no significant variations in the hydraulic setup between facilities. To complement these measurements, a measurement of initial ROI was also obtained from time-resolved x-ray radiography [45], which is discussed in more detail in the following

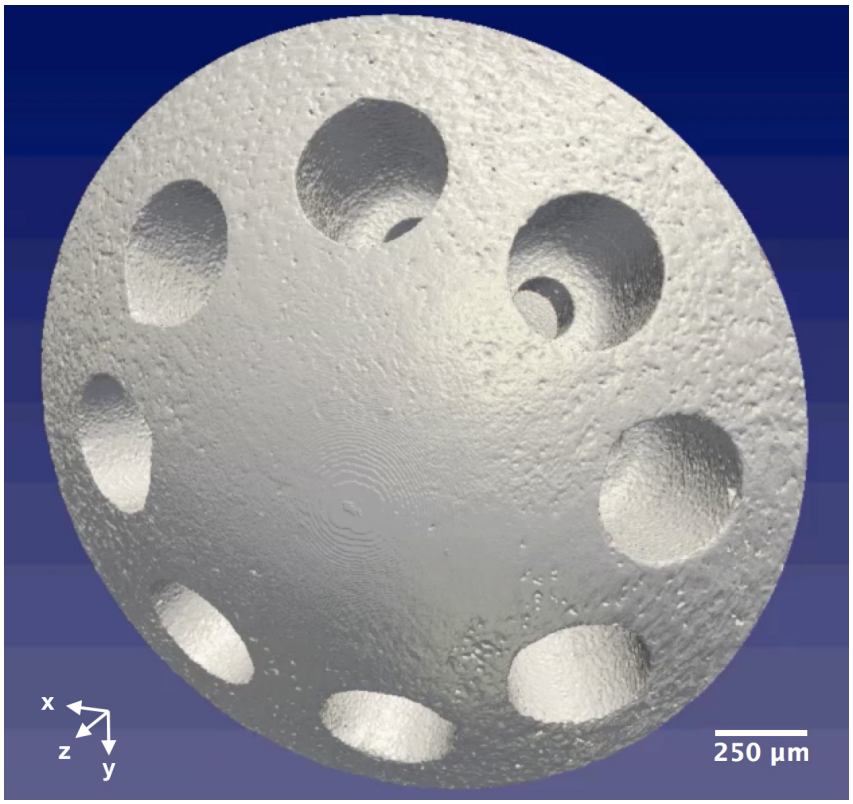

(a) Outer surface from x-ray tomography at Argonne.

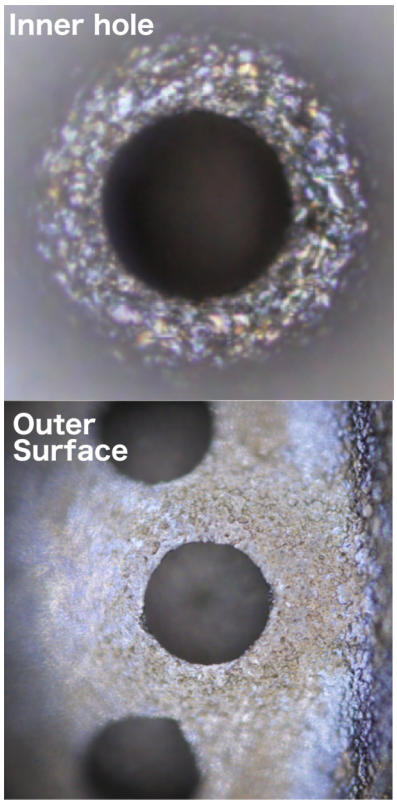

(b) Microscope images from Sandia.

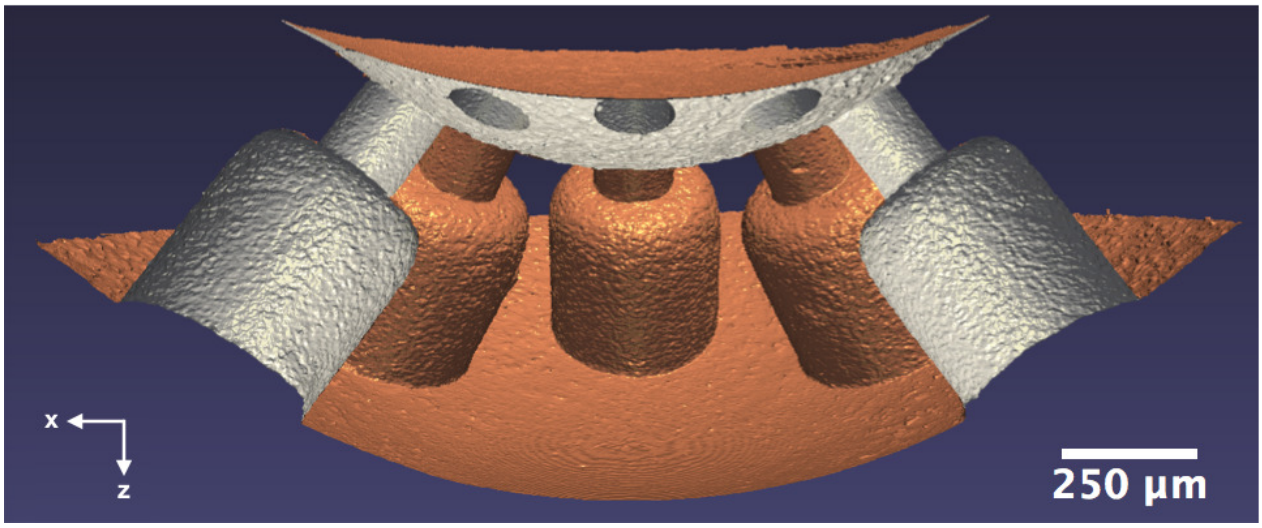

(c) Saggital plane from x-ray tomography at Argonne. False color indicates inner surface (orange) and outer surface (grey).

Figure 4: Isosurface of Spray G Injector #28 from Argonne tomography data (a,c) compared to optical microscopy (b).

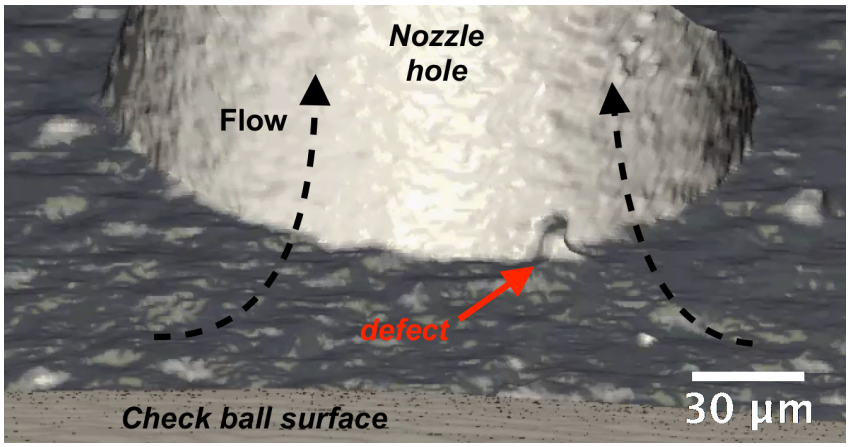

Figure 5: X-ray tomography isosurface inside the sac, showing a defect at the corner of a nozzle hole.

section. While the emerging tip of the spray is inside the measurement region, the total fuel injected can be integrated. The time derivative of this quantity provides an independent check of initial ROI.

Spray momentum (ROM) was determined using a test rig originally designed for measuring rate of momentum on Diesel injectors [18]. The injector was fitted in a test chamber with ambient pressures up to 100 bar, and a piezo-electric force sensor was aligned with the axis of the spray. When the spray from the injection event impacts the sensor, and under the hypotheses of perpendicular air entrainment and perpendicular projection of the spray after impact, the force registered by the sensor is the direct measurement of the momentum being given to the spray in the injection event. The spray momentum was measured using two different configurations [59]. Due to the low included angle, it was determined that the best method of measuring GDI injectors was a "frontal configuration", with the injector and the piezo-electric sensor in the same axis. All of the plumes from the injection event were collected simultaneously. Given that the plumes were not impacting the sensor perpendicularly, a correction was made to account for the angle between the plumes and the sensor normal axis. The injector holder was designed with a hydraulic circuit that allowed temperature control of the body of the injector. The ROM experiments shown in this work were performed with an injector body temperature of 90°C. However, rate of momentum measurements were checked for a range of temperatures (40-90)°C and it was noted that the values did not change outside the margin of errors of the measurement.

Figure 6b-c shows the ROM and ROI for all of the orifices of Spray G injector AV67-026. The radiography ROI data is taken for injector AV67-028. The error bars include both systematic and random experimental uncertainty and shot-to-shot variation at 95% confidence. We note an overshoot and oscillation at start of injection (SOI). For the ROM data, exaggeration of the overshoot may be explained by the change in aerodynamic resistance of the spray tip relative the fluid which follows behind. Once the spray has impacted the ROM sensor, this effect disappears. The overshoot is also partially explained by the needle lift profile (Fig. 6c); the needle position overshoots at SOI. However, the oscillations in the ROI (Fig. 6b) are consistently longer-lived than the needle overshoot, and vary between facilities and measurements. The shot to shot variation about the mean (indicated by the error bars) explains the variations during the steady-state region but does not explain the disagreement in the measurements just after SOI ($t < 0.2$ ms). Persistent transients in mass flux (due to oscillation of the fluid well after the needle position is at steady state) have been observed in diesel ROI measurements due to the needle hitting the travel stop and are often considered artificial [46, 70]. This explains why the radiography and rate meter data do not agree for $t < 0.2$ ms. However, the strong fluctuations in the radiography data suggest that this is not simply a measurement error. Moon et al. [71] have observed that multi-hole GDIs experience more pronounced transient fluctuations than diesel injectors, and propose that the low needle lift may be responsible for this phenomenon. Recent simulations [58] which reveal the complexity of the flow past the needle seat and in the sac support the hypothesis that GDIs exhibit strong and persistent transients in ROI under more realistic operating conditions. This is supported by the observation that the transients can vary significantly between different injectors with the same nominal geometry, while the transients for a particular injector are highly repeatable during subsequent

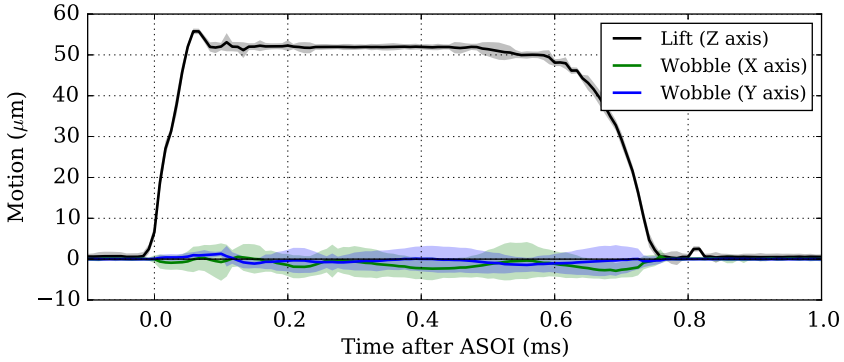

(a) Needle lift and wobble from x-ray imaging at Argonne.

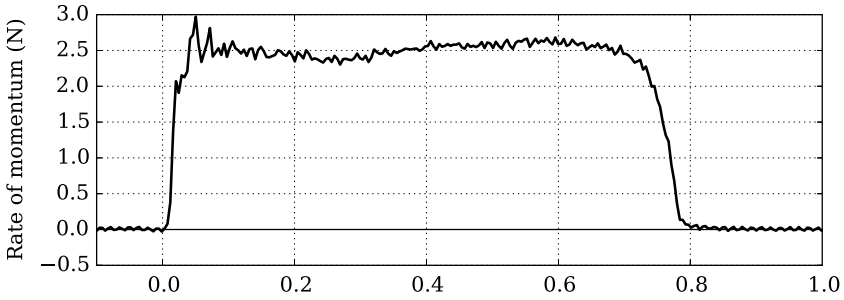

(b) Rate of momentum data from CMT.

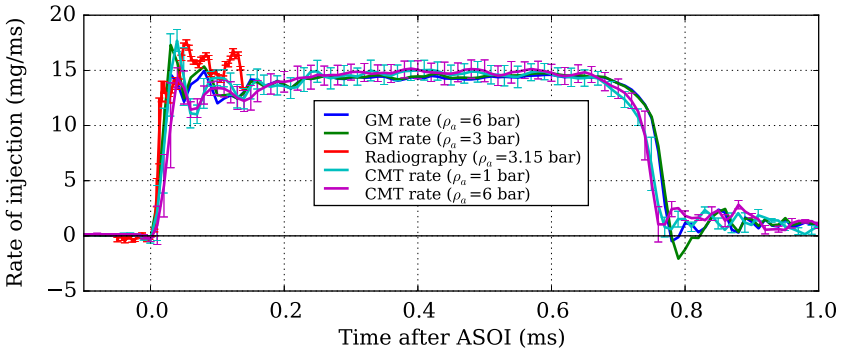

(c) Rate of injection data for injector #26 (CMT) and #28 (others).

Figure 6: Needle lift (a), ROI (b) and ROM (c) for short (680 μs command) injections. The colored bands in the needle lift plots indicate 99.7% confidence intervals. The error bars on the ROI data represent 95% confidence intervals including both measurement uncertainty and shot to shot variation.

tests. However, caution must be taken in the interpretation of SOI transients in ROI data. The measurements are sensitive to the injector clamping mechanism, which can vary between test facilities.

Figures 6a & 7a show that the needle wobble is small and has a relatively large uncertainty. The magnitude of the wobble is on the order of 2 to 4 μm. This corresponds to only one or two pixels of displacement in the x-ray images. The nominal minimum clearance between the sides of the needle and the guides (the maximum possible off-axis motion of the needle) is approximately 4 μm, so it is possible that the needle may be making physical contact with the guides. This will cause mechanical deflections which may affect ROI measurements. However, higher resolution measurements will be required to confirm this. The wobble does not cause any appreciable change in the flow area into the sac. However, the motion may lead to asymmetric and time-varying inflow to the sac. This is a matter of ongoing investigation [58].

3.3. Near-field spray structure and liquid penetration

Time-resolved x-ray radiography was used to quantitatively characterize the density distribution of the plumes near the nozzle. Measurements were performed at the 7-BM beamline of the APS at Argonne

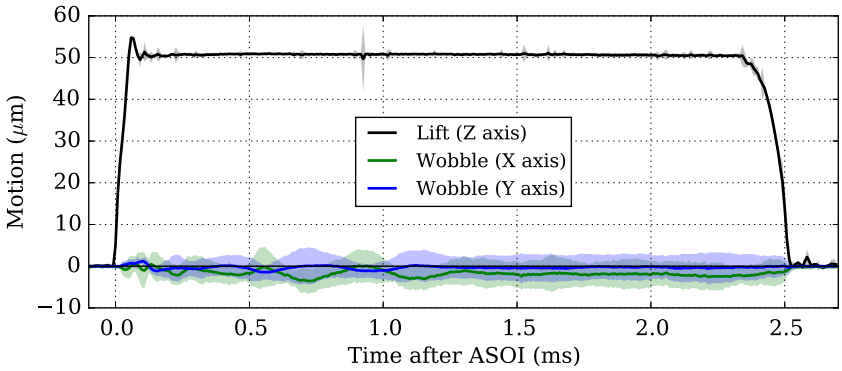

(a) Needle lift and wobble from x-ray imaging at Argonne.

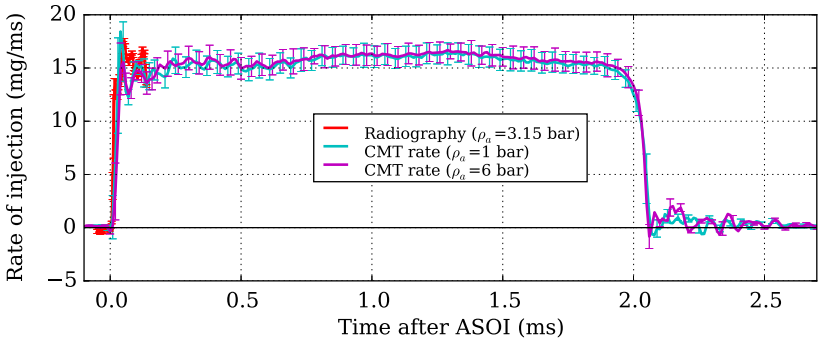

(b) Rate of injection data for injector #26 (CMT) and #28 (Argonne).

Figure 7: Needle lift (a) and ROI (b) for longer (2.0 to 2.5 ms) injections. The colored bands in the needle lift plots indicates 99.7% confidence intervals. The error bars on the ROI data represent 95% confidence intervals including both measurement uncertainty and shot to shot variation.

[61] under the non-evaporative conditions listed in Table 1. The principles of x-ray radiography and the experimental facility at Argonne are discussed at length in previous publications [44, 45, 72]. In brief, a monochromatic x-ray beam of mean energy 8 keV is focused to a 5 μm $\times$ 6 μm (full width at half maximum) spot using a pair of x-ray focusing mirrors. The beam passes through a line of sight in the spray and the transmission of x-rays is recorded on a fast PiN diode. By translating the spray through the fixed beam, a time-resolved, ensemble-average distribution map of the spray is obtained. The projected mass (M, mass per unit area) along the line of sight is computed from the recorded intensity I via the Lambert-Beer law;

$$M\ (\mu\mathrm{g/mm}^2) = \frac{-1}{\mu} \log \frac{I}{I_0} = \int \rho_{\mathrm{fuel}}\, dz \tag{1}$$

where I_0 is a reference intensity and μ is the relative absorption coefficient of the liquid fuel, adjusted to allow for displacement of the ambient gas in the chamber. The absorption coefficient is determined via calibration against air and water in a cuvette.

Radiography data are shown in Figures 8a-b, averaged over the relatively steady portion of the injection (0.25 to 2 ms after SOI). Fig. 8a, shows the 'primary' rotation view at $\theta = 0°$ with the electrical connector of the injector facing out of the page and the y and z axes defined as per the JSAE 2715 standard [60]. Fig. 8b shows the 'secondary' view with $\theta = -22.5°$, where the electrical connector is tilted upward and out of the page.

A key feature of note in these GDI injectors relative to diesel sprays [45] is the rapid drop-off in projected mass with distance from the injector orifice due to rapid mixing with the ambient [73]. This can be quantified by measuring the evolution of the mass-averaged velocity of the spray. During steady state, the projected mass from x-ray radiography can be used to measure the relative change in the mass-averaged velocity V_{ma} by comparing the transverse integrated mass (TIM) of the spray at some axial location z to the value at the

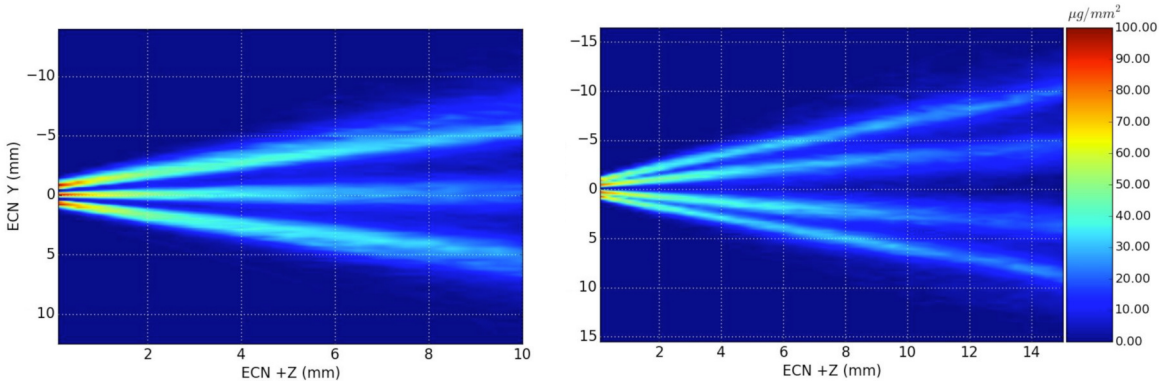

(a) Primary orientation; 0° rotation in z, 0.5 ms after SOI.

(b) Secondary orientation; -22.5° rotation in z, 0.5 ms after SOI.

Figure 8: X-ray radiography measurements of projected fuel mass for Spray G from two projection angles.

nozzle exit [74];

$$\frac{V_{ma}(z,t)}{V_e} = \frac{\mathrm{TIM}(0,t)}{\mathrm{TIM}(z,t)}, \tag{2}$$

$$\mathrm{TIM}(z,t)\ (\mu\mathrm{g/mm}) = \int M(y,z,t)dy. \tag{3}$$

At steady state, there is no accumulation of mass in the domain, so changes in the time-average steady-state TIM can be directly related to relative change in mass-averaged axial velocity with axial position [74]. The results are shown in Figure 9. A non-dimensional length scale is used on the horizontal axis to account for variations in the ambient to liquid density ratio (ρ_a/ρ_l) and effective jet diameter d_{eff};

$$Z^* = \frac{z}{d_{\mathrm{eff}}}\sqrt{\frac{\rho_a}{\rho_l}}. \tag{4}$$

This length scaling is typically used to describe the evolution of turbulent gas jets [75]. Kastengren et al. [74] have shown that under some conditions it can be used to collapse the effects of density ratio on spray width for diesel sprays. The effective diameter is determined by the geometric diameter and exit area coefficient $d_{\mathrm{eff}} = d_0 C_a$ [76], where C_a has been measured by Payri et al [19]. The data in Fig. 9 are compared to the same quantity measured for the ECN Spray A single-hole diesel injectors, which were operated at 1500 bar injection pressure and 20 bar ambient pressure with n-dodecane at room temperature [45, 51]. In non-dimensional terms, the velocity decay rate is approximately 4 times faster for Spray G than for Spray A. The steady state absolute exit velocities V_e for Spray G are 104 ± 3 m/s, compared to 553 ± 6 m/s for the Spray A injectors [45]. This velocity is calculated from the rate of injection and TIM values at 0.1mm from the nozzle exit. The exit velocity is much lower than the ideal value, implying an average hole discharge coefficient of 0.48 ± 0.02.

Liquid penetration measurements for Spray G are shown in Fig. 10. We compare the x-ray radiography to DBI and Mie scattering measurements [24]; good agreement was observed within the uncertainty ranges of each. The data have been corrected for the out-of-plane angle of the central plume, which was calculated as a function of time from the full width at half maximum of the x-ray radiography measurements. The liquid penetration is defined as the point at which the transverse integrated mass (TIM) reaches a threshold of 25% of the maximum value [45]. This threshold is set to account for the rapid decrease of density with axial position and the high background level of fuel around the leading edge of the spray. Although the spray consists of eight closely-spaced plumes, the leading edge of the spray is more diffuse than the upstream regions because of plume-to-plume variations in penetration speed.

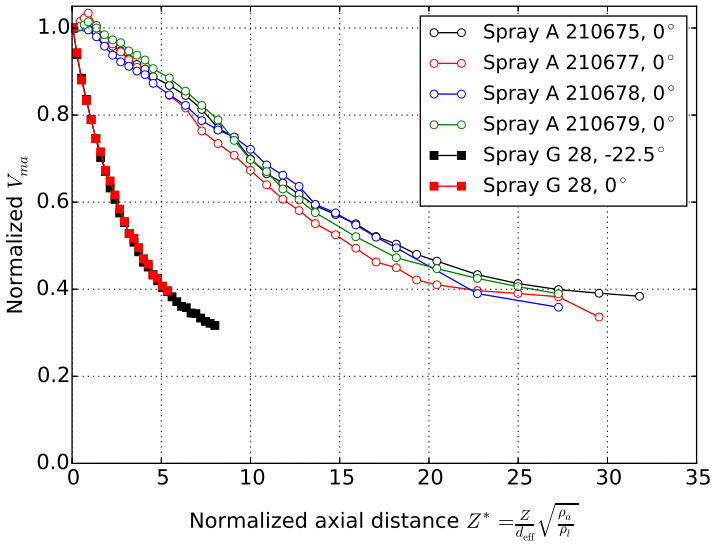

Figure 9: Normalized velocity decay profiles for Spray G (solid squares) compared to the ECN Spray A diesel injector [45, 51] at P_{inj} =1500 bar, P_{amb} =20 bar (open circles).

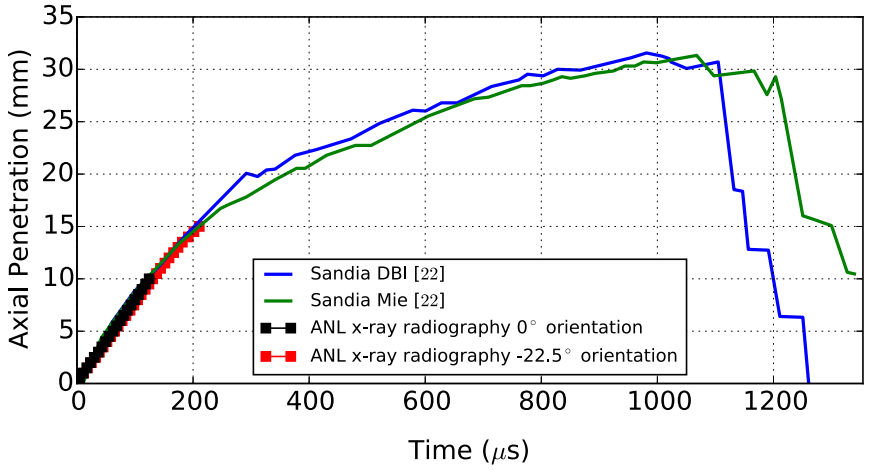

Figure 10: Spray G liquid penetration measurements from x-ray radiography (solid squares), DBI and Mie scattering [24].

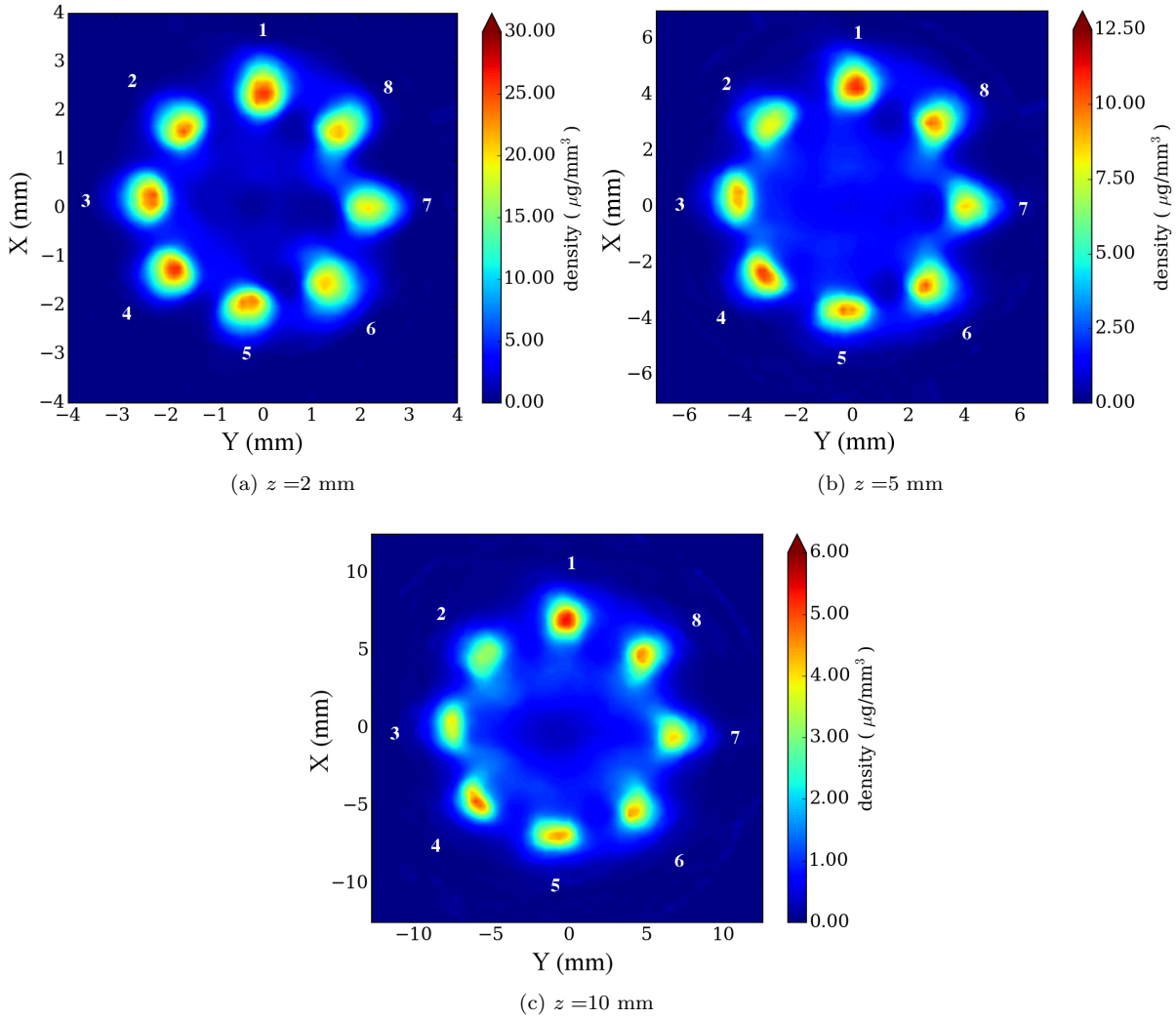

(a) z =2 mm

(b) z =5 mm

(c) z =10 mm

Figure 11: X-ray radiographic tomography of density field in $x-y$ planes, temporally averaged from t=0.17 to 2.4ms.

3.4. Plume-to-plume variation and spray targeting

Due to the close spacing of the 8 holes, only 3 or 4 plumes are visible from any line of sight, as some of the 8 plumes will always overlap. In order to isolate individual plumes, x-ray tomographic radiography was employed [48]. The injector was scanned horizontally at three planes in z (2, 5, 10 mm) and rotated through 180°. A penalized maximum likelihood algorithm [62] was used to reconstruct the quantitative time-resolved, ensemble-average density fields for long (2.5ms) injections [77]. The three tomography planes are shown in Fig. 11, averaged over the steady part of the injection. The hole numbers are indicated on the plot, with the electrical connector pointing upward and the plume velocity heading into the page.

The major feature of note in Fig. 11 that is not apparent in the planar radiography (Fig. 8a-b) is that the left-side plumes (1-5) have higher peak densities than the right-side plumes (6-8). As the density field is computed tomographically from projections of the spray made from multiple angles, there is no spatial bias in the reconstruction that might generate such an asymmetry artifically. The plume shapes are also slightly nonuniform, suggesting weak asymmetry. This was quantified by computing both the total plane TIM (eqn. 3) and the TIM for the individual plumes; $\mathrm{TIM}_{\mathrm{plume}}$ (μg/mm) $= \int \rho \, dA_{\mathrm{plume}}$. The plume centroids were located and circular regions of equal size were integrated around each plume, capturing at least 95% of the total mass. This method was chosen in order to isolate the spray plume cores from the liquid which accumulates in the space between the plumes over time. The TIM data are shown as a function of time in Fig. 12a. The spread from highest to lowest plume is significant, being about ±17% of the mean.

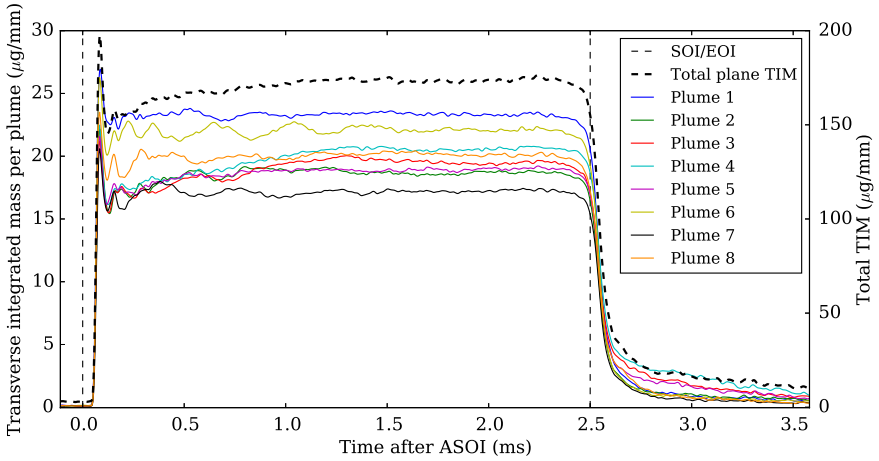

(a) Transverse integrated density per plume (solid lines, left vertical axis) and total (dashed line, right vertical axis).

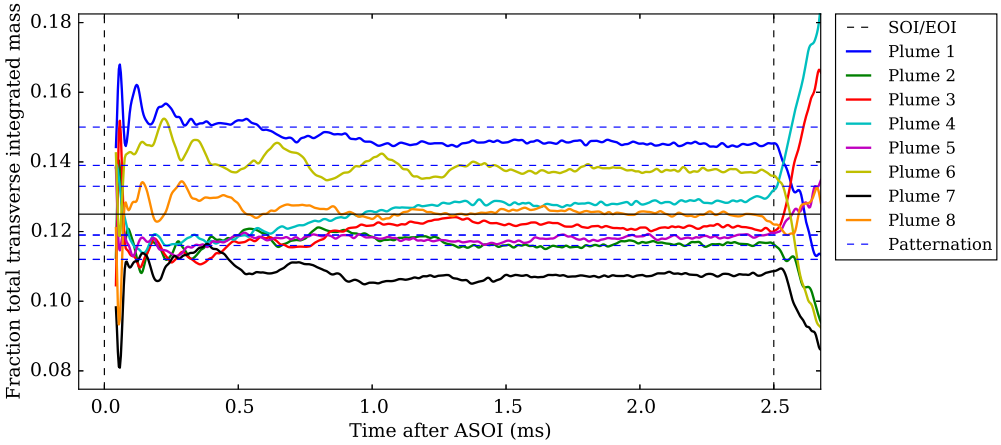

(b) Fraction of transverse integrated density per plume (solid lines), compared to mechanical patternation (blue dashed lines).

Figure 12: Distribution of transverse integrated density beween plumes at $z = 2$ mm in absolute and fractional terms, determined from x-ray radiographic tomography. Vertical dashed lines indicate start and end of commanded injection.

We also normalized the TIM values by the total to obtain a fractional distribution of the injected mass into each plume; this is shown in Fig. 12b. The weakest plume has 11% of the total mass, and the strongest has 15%. Fig. 12b also shows time-averaged mechanical patternation data supplied by Delphi for this injector (horizontal dashes). The patternation data were collected much further downstream (50 mm vs. 2 mm for the radiography), and measure mass flux rather than density. However, the measurements correlate well; the per-plume spread in mass flux from patternation is very close to the per-plume spread in TIM.

There is no statistically significant correlation between the distribution of TIM between the plumes (Fig. 12) and the diameters of the inner holes (Tab. 2). This may be due to the small sample size, but it suggests that the hole discharge coefficients are unequal, not just that the hole sizes vary. The mechanism behind this variation is not yet fully understood, as there is presently insufficient information to be able to quantify the individual holes' discharge coefficients, which may vary during the injection event. Recent modeling efforts suggest that strong vortical structures in the sac may play an important role [58]. Further investigation with a larger sample size (more injectors) will be required to determine whether a significant correlation exists.

Fig. 12 also reveals transient oscillations in the TIM, particularly for holes 1, 6, 7 & 8. The total TIM (Fig. 12a) does not oscillate, but rises steadily with time. It is likely that this oscillation is not throttling, but rather a disturbance of the flow in the sac that creates a transient imbalance in per-plume mass flow.

The angles of the plume centers relative to the z (injector body) axis were measured at the three tomography plane locations by tracking the plume centroids from the inner hole entrance plane. Here, we define 'plume angle' as the angle between a line from the hole axis at the exit plane to the plume's center of mass at a given axial distance to the z axis of the injector body. This refers to the targeting of a plume with

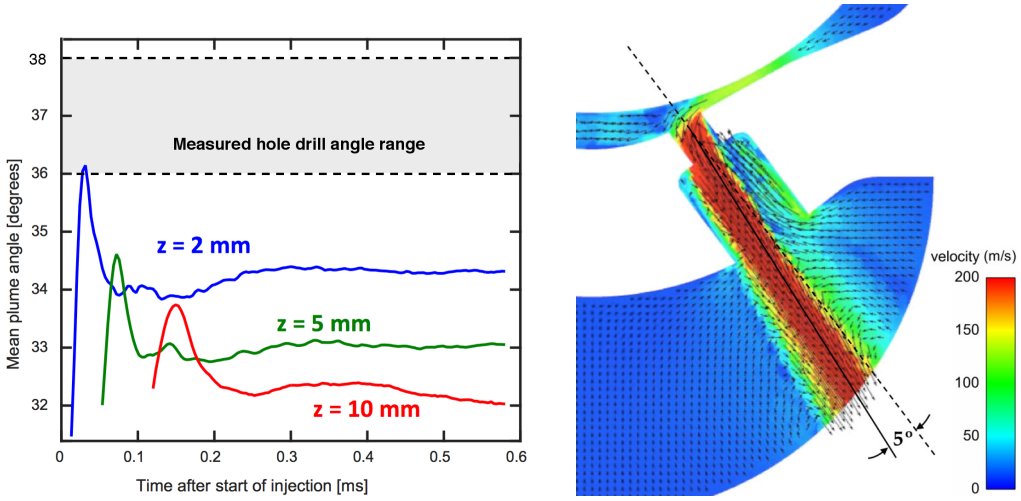

(a) Plume-averaged vectoring of sprays from x-ray radiography data at three axial distances from the nozzle, comparing to hole drill angle range.

(b) Compressible HRM k-ϵ simulation of a Spray G plume, showing the deviation of plume and drill angles.

Figure 13: Vectoring of plumes from x-ray radiography (a), and comparison with numerical simulation (b).

respect to the injector body axis , and is not to be confused with the cone angle (spreading of an individual plume). Averaging across all 8 plumes, Figure 13a shows that the plume angles relative to the axis of the injector body are consistently smaller than the drill angles (Tab. 2). The plumes also tend to bend inward as distance from the nozzle increases.

We propose that there are two phenomena causing this reduction in plume angle. The reduction in angle with distance from the nozzle suggests an entrainment-driven effect, possibly due to lower pressure in the core of the spray. The large difference in angle nearer to the injector relative to the hole drill angle may be explained by simulation results of the flow inside the nozzle holes. Figure 13b shows a cut-plane of velocity through one hole of Spray G. The simulation was performed using a homogeneous relaxation model (HRM) with compressible three-phase flow (liquid and vapor fuel, and non-condensable ambient gas) and a k-ϵ turbulence model. Further details may be found in previously published work [78]. The simulation shows separation of the flow from the nozzle wall due to the large turning angle. The hole L/D is sufficiently short that the flow does not straighten before it exits the hole, and as such the momentum is angled inward by approximately 5° relative to the drill angle. Similar results have been obtained from other simulations [79, 80]. The x-ray measurements were conducted at a lower temperature than the Spray G specification (Tab. 1). Since spray collapse is a strong function of temperature, we need to investigate whether the same phenomenon occurs at higher temperatures. This is discussed in the following section.

3.5. Spray entrainment and mixing measurements

To study the behavior of Spray G under the nominal conditions (Table 1), phase-doppler interferometry (PDI) measurements were conducted by GM R&D, and these were compared against diffuse backlit illumination (DBI) images of the spray collected at Sandia National Laboratories. The results are shown in Figure 14. PDI data were collected along a radial profile 15 mm downstream of the nozzle, as indicated by Figure 14a. Both axial and radial velocity components of the plumes were measured in space (horizontal axes) and time (vertical axes). The radial profiles (Fig 14b-c) reveal a time-dependent shift in the location of peak velocity (indicated on the plots by the arrows). This indicates an inward movement of the plumes as the injection proceeds.

To confirm that the movement of the peak velocity was indicative of a movement of the spray axis, the plume angles were also calculated as a function of time from the DBI measurements. Fig. 14e shows a sample DBI image, at 0.448 ms after SOI. The plume axes are indicated by the blue lines. For the DBI measurements, the nozzle was rotated 22.5° in the z axis to the 'secondary' orientation, as per Fig. 8b. The radial position of the plume at 15 mm from the DBI data has been overlaid on the PDI velocity magnitude

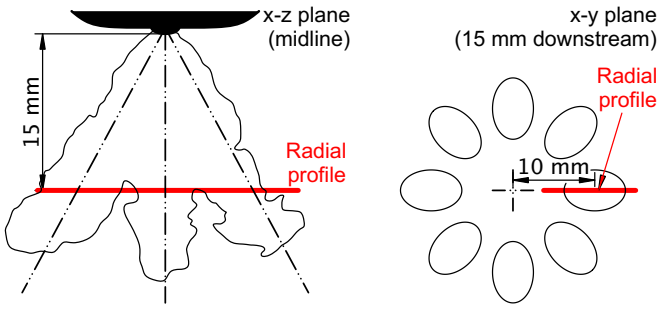

(a) Diagram of spray, showing location of the PDI measurement in the 'primary' orientation.

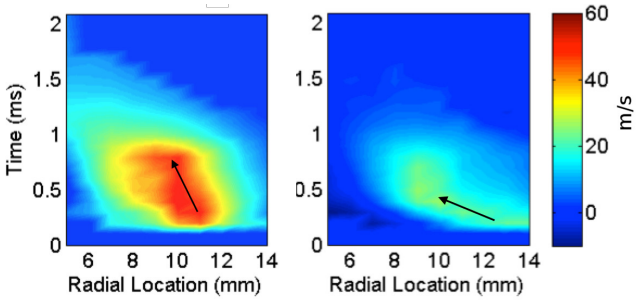

(b) Radial profile, axial velocity

(c) Radial profile, radial velocity

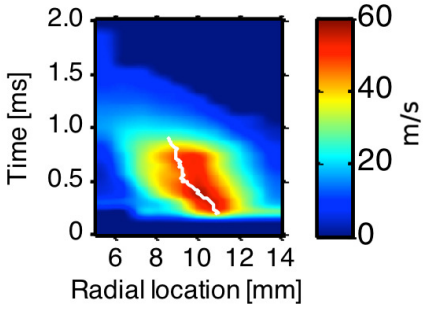

(d) Radial profile, velocity magnitude. The white line indicates the plume position from DBI data at the same position.

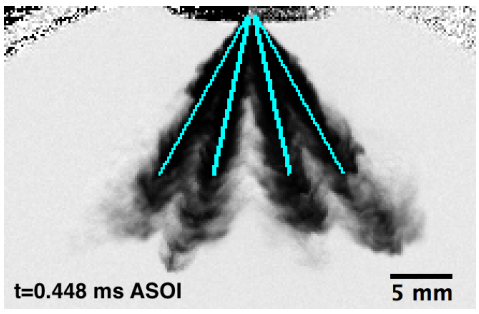

(e) DBI image of spray at 0.448 ms after SOI. The nozzle has been rotated 22.5° in z to the 'secondary' orientation. The plume directions are shown by the lines.

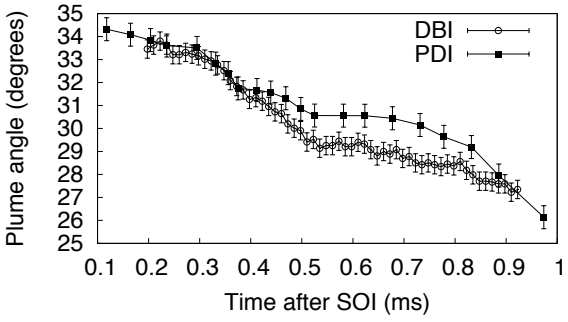

(f) Plume angle vs. time after SOI, as measured by DBI (Injector AV67-028) and PDI (Injector AV67-016) , 15 mm from the nozzle.

Figure 14: DBI and PDI measurements of plume angle and velocity at $z = 15$ mm from the nozzle.

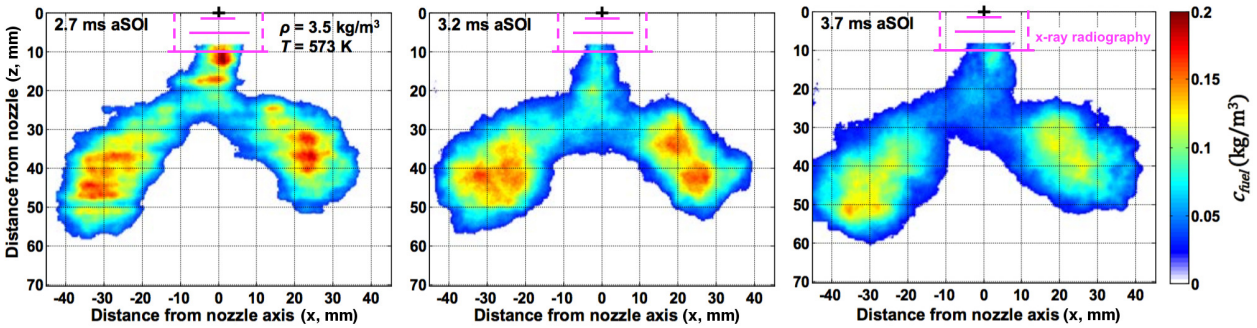

Figure 15: LIF measurements of Spray G at nominal conditions, at three times after EOI. The + mark at x, z=0,0 indicates the location of the injector tip. The solid magenta lines indicate the x-ray tomography planes shown in Fig. 11, and the dashed lines indicate the extent of the x-ray radiography measurement in Fig. 8.

in Fig. 14d (the DBI data is indicated by the white line). From this data, a plume angle vs. time was calculated for both datasets and is shown in Fig. 14f. The peak velocity magnitude at each time has been used as the angle reference for the PDI data. We see a strong correlation between the peak velocity radius and the plume axis radius. Both measurements are decreasing with time, indicating inward motion of the plumes. The angle is more acute than the drill angle, indicating inward motion. The reduction in angle is larger than the lower-temperature x-ray measurements in Fig. 13a.

Under the conditions shown in Fig. 14, the plume angle is observed to be decreasing (Fig. 14f) while the rate of injection (Fig. 6c) is relatively steady. A likely explanation for this behavior is that fuel is being transported into the space between the plumes due to entrainment of the ambient gas.

The effect of uneven plume-to-plume mass distribution on the later evolution of the spray was revealed by laser-induced fluorescence (LIF) measurements in Figure 15. The data were collected at IFP Energies Nouvelles (France). The experimental methodology has been reported elsewhere [81] and therefore only a brief summary is presented here. The experiments were carried out in a high pressure vessel where a pre-combustion was used to reach Spray G ambient conditions. A fluorescent tracer, p-difluorobenzene, was added to the iso-octane fuel in small proportions (0.03% v/v). Its fluorescence was excited by a 266 nm laser sheet entering the vessel through a side window illuminating plumes 1 and 5 in the $x - z$ plane . An intensified ICCD camera equipped with a 292 ± 14 nm bandpass filter placed at 90° was used for collection.

Measurements taken at several times after the end of injection (Fig. 15) for a single spray event reveal two important phenomena. Near the nozzle ($z < 20$ mm), spray collapse effects are dominant, as evidenced by the narrow spreading angle. We observe that the late collapse of the spray is consistent with the decreasing plume angle measured earlier in the injection (see Fig. 14f). Collapse of the spray after the end of injection is distinct from collapse of the plumes during injection, as it is driven primarily by the momentum of the injected charge in the far field and the resulting entrainment, rather than the dynamics of the plumes in the near field. The second phenomenon of note in Fig. 15 is that that the mass distribution is consistently skewed in the $-x$ direction. The asymmetries correlate with variations in plume density measured much closer to the nozzle (Fig. 12). We propose that these variations promote an uneven distribution of fuel, which are amplified by mixing and entrainment, and continue to dominate the mixing process well after the end of injection. These mixing variations can in turn have a measurable effect on combustion; Blessinger et al. [23] have shown how this can affect equivalence ratio. Observations drawn from Fig. 15 are preliminary, as more data is needed to understand the significance of shot to shot variation on the post-injection mixing process. This is a matter of ongoing research.

4. Conclusions

In this paper, the results of a range of experimental measurements of the ECN Spray G injector have been summarized. By comparing the results obtained by various measurement techniques across a standard platform under operating conditions which are kept as consistent as possible, a number of new findings are reported which were not evident from the study of the individual experiments in isolation:

1. High-resolution measurements of the internal geometry revealed variations of 2% in the inner hole diameters, 20% variation in L/D ratio, and 4% variation in minimum cross-section area. Defects of approximately 10 μm in size were observed in critical regions of the hole geometry, such as at the inlet corners to the nozzles.
2. X-ray radiography measurements indicate that the integrated density of the plumes can vary by up to ±17% about the mean value, with the weakest plume having only 11% of the total integrated density and the strongest having 15%.
3. The plume-to-plume density variations revealed by X-ray radiography show no obvious correlation with variations in the hole geometry.
4. X-ray radiography revealed that the spray's mass average velocity decays approximately 4 times faster (in non-dimensional terms) than the Spray A diesel injector. It remains a matter for future work to determine how the closely-spaced nature of the plumes affects penetration development.
5. The plumes' centers of mass had targeting angles up to 5° smaller than the hole drill angles with respect to the injector body axis . Simulations suggest that this is due to the radial momentum of the flow entering the hole from the sac, which is highly asymmetric. It is possible that the holes are not completely filled with liquid, and this implies that the boundary conditions at the holes are complex.
6. The plumes were found to have a decreasing targeting angle with increasing distance from the nozzle and increasing duration of injection. DBI, PDI and x-ray radiography data all reveal a time-dependent motion of the plumes toward the nozzle centerline. This agrees with the decrease in momentum flux over time reported by Payri et al [59]. The effect is stronger at higher temperature. Since the spray targeting and rate of injection remain constant, this indicates that fluid is moving toward the centerline. This suggests the presence of a low-pressure region between the plumes, which may promote spray collapse. As a result, the spray does not have a true 'steady state'.

The reduced included angles between the plumes, the increased mixing with both time and distance from the nozzle, and the bias in included angle due to the vectoring of the plumes at the hole exits are factors than could contribute to the phenomenon of spray collapse. With larger injection durations and penetration depths, the probability of spray collapse will increase.

The ECN Spray G injectors were selected to be representative of typical GDI designs, and the specific injectors were selected from a matched set based on their patternation and ROI performance. It is likely that many of the off-design behaviors observed in Spray G are typical of many GDIs, rather than being unique to these injectors. The effects of small-scale geometric deviations and hole to hole variations indicate that the internal flow is complex and the nozzle exit boundary conditions are complex and time-varying. This points toward the need for transient simulation efforts which include the details of the internal nozzle geometry.

Acknowledgements

The authors would like to acknowledge all the contributors to the ECN Spray G work presented at the Fourth International Workshop of the Engine Combustion Network, which was held at the University of Kyoto in Kyoto, Japan, September 2015. The authors thank Delphi for supplying the injectors and control equipment used in the Spray G activities.

The authors gratefully acknowledge the computing resources provided on the Blues and Fusion high-performance computing clusters operated by the Laboratory Computing Resource Center at Argonne National Laboratory.

The x-ray experiments were performed at the 7-BM and 32-ID beam lines of the APS at Argonne National Laboratory. Use of the APS is supported by the U.S. Department of Energy (DOE) under Contract No. DE-AC02-06CH11357.

Research was also performed at the Combustion Research Facility, Sandia National Laboratories, Livermore, California. Sandia National Laboratories is managed and operated by National Technology and Engineering Solutions of Sandia LLC, a wholly owned subsidiary of Honeywell International, Inc., for the U.S. Department of Energy?s National Nuclear Security Administration under contract DE-NA-0003525.

Argonne and Sandia National Laboratories' fuel spray research is sponsored by the DOE Vehicle Technologies Program, under the direction of Gurpreet Singh and Leo Breton.

References

[1] K. K. Kuo, P. Zarchan (Eds.), Recent Advances in Spray Combustion: Spray Atomization and Drop Burning Phenomena, Vol. I, Vol. 166 of Progress in Astronautics and Aeronautics, AIAA, 1996.

[2] M. A. Shost, M. C. Lai, B. Befrui, P. Spiekermann, D. L. Varble, GDi Nozzle Parameter Studies Using LES and Spray Imaging Methods, SAE Paper 2014-01-1434.

[3] T. Kim, S. Park, Effects of Spray Patterns on Mixture Formation Process in Multi-hole-type Direct Injection Spark Ignition (DISI) Gasoline Engine, Atom. Sprays (2015) 1–37.

[4] B.-Q. He, J.-X. Wang, J.-M. Hao, X.-G. Yan, J.-H. Xiao, A study on emission characteristics of an EFI engine with ethanol blended gasoline fuels, Atmospheric Environment 37 (7) (2003) 949–957.

[5] M. Zhang, M. C. Drake, K. Peterson, Simultaneous High-Speed Imaging of Fuel Spray, Combustion Luminosity, and Soot Luminosity in a Spray-Guided Direct Injection Engine With Different Multi-Hole Fuel Injectors, in: Proceedings of the ASME 2013 Internal Combustion Engine Division Fall Technical Conference ICEF2013, Vol. 19066, Dearborn, Michigan, 2013.

[6] S. Lee, S. Park, Spray atomization characteristics of a GDI injector equipped with a group-hole nozzle, Fuel 137 (2014) 50–59.

[7] N. I. Kolev, Fragmentation and coalescence dynamics in multiphase flows, Exp. Therm. Fluid Sci. 6 (3) (1993) 211–251.

[8] M. Krämer, E. Kull, M. Heldmann, M. Wensing, Investigations on Gasoline Spray Propagation Behaviour Characteristic for Multihole Injectors, in: SAE Technical Paper, 2014, pp. 2014–01–2732.

[9] R. Payri, F. J. Salvador, P. Martí-Aldaraví, D. Vaquerizo, ECN Spray G External Spray Visualization and Spray Collapse Description through Penetration and Morphology Analysis, Applied Thermal Engineering 112 (2017) 304–316. doi:10.1016/j.applthermaleng.2016.10.023.

[10] J. Lee, K. Nishida, M. Yamakawa, An Analysis of Ambient Air Entrainment into Split Injection D.I. Gasoline Spray by LIF-PIV Technique, SAE Technical Paper (2002) 2002–01–2662.

[11] D. W. Morris, P. J. Bowen, S.-I. Kwon, Influence of ambient pressure on transient air-assist automotive fuel sprays, in: IMechE Conference Transactions, London, UK, 2003, pp. C610–021–2003.

[12] A. Arbeau, R. Bazile, G. Charnay, A new application of the particle image velocimetry (piv) to the air entrainment in gasoline direct injection sprays, SAE Technical Paper (2004) 2004–01–1948.

[13] G. Zhang, D. L. S. Hung, Temporal investigations of transient fuel spray characteristics from a multi-hole injector using dimensionless analysis, Exp. Therm. Fluid Sci. 66 (2015) 150–159.

[14] J. Serras-Pereira, Z. van Romunde, P. G. Aleiferis, D. Richardson, S. Wallace, R. F. Cracknell, Cavitation, primary break-up and flash boiling of gasoline, iso-octane and n-pentane with a real-size optical direct-injection nozzle, Fuel 89 (9) (2010) 2592–2607.

[15] J. Lacey, F. Poursadegh, M. J. Brear, R. Gordon, P. Petersen, C. Lakey, B. Butcher, S. Ryan, Generalizing the behavior of flash-boiling, plume interaction and spray collapse for multi-hole, direct injection, Fuel 200 (2017) 345–356. doi:10.1016/j.fuel.2017.03.057.

[16] M. Furuyama, A visualization of spray of gasoline injection, SAE Technical Paper (1990) 901606.

[17] V. Sick, M. C. Drake, T. D. Fansler, High-speed imaging for direct-injection gasoline engine research and development, Exp. Fluids 49 (4) (2010) 937–947.

[18] R. Payri, J. García, F. Salvador, J. Gimeno, Using spray momentum flux measurements to understand the influence of diesel nozzle geometry on spray characteristics, Fuel 84 (5) (2005) 551–561.

[19] R. Payri, J. Gimeno, P. Marti-Aldaravi, D. Vaquerizo, Momentum Flux Measurements on an ECN GDi Injector, SAE Technical Paper (2015) 2015–01–1893.

[20] J. M. Nouri, J. H. Whitelaw, Spray characteristics of a gasoline direct injector injector with short durations of injection, Exp. Fluids 31 (4) (2001) 377–383.

[21] G. Wigley, M. S. Goodwin, G. Pitcher, Fuel breakup and atomization in the near nozzle region of a GDI injector, in: IMechE Conference Transactions, London, UK, 2003, pp. C610–019–2003.

[22] N. Mitroglou, J. M. Nouri, Y. Yan, M. Gavaises, C. Arcoumanis, Spray Structure Generated by Multi-Hole Injectors for Gasoline Direct-Injection Engines, SAE Paper (2007) 2007–01–1417.

[23] M. Blessinger, J. Manin, S. A. Skeen, M. Meijer, S. Parrish, L. M. Pickett, Quantitative mixing measurements and stochastic variability of a vaporizing gasoline direct-injection spray, Int J Engine Res 16 (2) (2015) 238–252.

[24] J. Manin, Y. Jung, S. Skeen, L. M. Pickett, S. E. Parrish, L. E. Markle, Experimental characterization of di gasoline injection processes, SAE Paper (2015) 2015–01–1894.

[25] L. M. Pickett, J. Manin, R. Payri, M. Bardi, J. Gimeno, Transient Rate of Injection Effects on Spray Development, in: ICE2013, SAE International, 2013, pp. 2013–24–0001.

[26] M. Yamakawa, S. Isshiki, J. Lee, K. Nishida, 3-D PIV Analysis of Structural Behavior of D.I. Gasoline Spray, SAE Technical Paper (2001) 2001–01–3669.

[27] G. Rottenkolber, J. Gindele, J. Raposo, K. Dullenkopf, W. Hentschel, S. Wittig, U. Spicher, W. Merzkirch, Spray analysis of a gasoline direct injector by means of two-phase PIV, Exp. Fluids 32 (6) (2002) 710–721.

[28] M. Yamakawa, D. Takaki, T. Li, Y.-y. Zhang, K. Nishida, Quantitative measurement of liquid and vapor phase concentration distributions in a d.i. gasoline spray by the laser absorption scattering (las) technique, SAE Technical Paper (2002) 2002–01–1644.

[29] F. Beyrau, A. Brauer, T. Seeger, A. Leipertz, Gas-phase temperature measurement in the vaporizing spray of a gasoline direct-injection injector by use of pure rotational coherent anti-Stokes Raman scattering, Opt. Lett. 29 (3) (2004) 247–249.

[30] J.-F. Le Coz, L. Hermant, Quantification of fuel concentrations and estimation of liquid/vapor ratios in direct injection sprays by laser-induced fluorescence, SAE Technical Paper (2001) 2001–01–0916.

[31] J.-F. Le Coz, C. Lemenand, G. Bruneaux, Gasoline injection and spray combustion in a cell with conditions typical of direct injection engines, SAE Technical Paper (2003) 2003–01–3108.

[32] M. Anbari Attar, M. R. Herfatmanesh, H. Zhao, A. Cairns, Experimental investigation of direct injection charge cooling in optical GDI engine using tracer-based PLIF technique, Exp. Therm. Fluid Sci. 59 (2014) 96–108.

[33] P. Rogler, R. Grzeszik, S. Arndt, M. Aigner, 3D analysis of vapor and liquid phase of GDI injectors using laser induced exciplex fluorescence tomography in a high pressure/high temperature spray chamber, SAE Journal 1 (2007) 2007–01–1827.

[34] G. Wigley, G. K. Hargrave, J. Heath, A High Power, High Resolution LDA/PDA System Applied to Gasoline Direct Injection Sprays, Part. Part. Syst. Charact. 16 (1999) 11–19.

[35] S. Alfuso, L. Allocca, F. E. Corcione, G. Valentino, G. Caputo, Droplets size and velocity in a gdi spray by pda and laser light extinction techniques, SAE Technical Paper (2001) 2001–01–047.

[36] G. Wigley, M. Goodwin, G. Pitcher, D. Blondel, Imaging and PDA analysis of a GDI spray in the near-nozzle region, Exp. Fluids 36 (4) (2004) 565–574.

[37] N. Mitroglou, J. M. Nouri, M. Gavaises, Spray characteristics of a multi-hole injector for direct-injection gasoline engines, Int. J. Engine Res. 7 (3) (2006) 255–270.

[38] P. G. Aleiferis, J. Serras-Pereira, Z. van Romunde, J. Caine, M. Wirth, Mechanisms of spray formation and combustion from a multi-hole injector with E85 and gasoline, Combustion and Flame 157 (4) (2010) 735–756.

[39] Y. Li, H. Guo, X. Ma, J. Wang, H. Xu, Droplet dynamics of DI spray from sub-atmospheric to elevated ambient pressure, Fuel 179 (C) (2016) 25–35.

[40] M.-C. Lai, Y. Zheng, M. Shost, X. Xie, A. Matsumoto, J. Wang, X. Zhang, S. Moon, J. Gao, K. Fezzaa, L. Zigan, I. Schmitz, M. Wensing, A. Leipertz, Characterization of Internal flow and Spray of Multihole DI Gasoline Spray using X-ray Imaging and CFD, SAE Journal 1 (2011) 2011–01–1881.

[41] L. Allocca, S. Dabagov, D. Hampai, L. Marchitto, S. Alfuso, Tomography of a GDI Spray by PolyCO Based X-Ray Technique, in: Proceedings of the ICE2013 11th International Conference on Engines & Vehicles, SAE International, Capri, Italy, 2013, pp. 2013–24–0040–8.

[42] L. Marchitto, S. B. Dabagov, L. Allocca, D. Hampai, A. Liedl, S. Alfuso, X-ray tomography of high pressure fuel spray by polycapillary optics, in: A. Khounsary, S. Goto, C. Morawe (Eds.), Advances in X-RayEUV Optics and Components VIII, Proc. of SPIE, SPIE, 2013, p. 884808.

[43] L. Marchitto, D. Hampai, S. B. Dabagov, L. Allocca, S. Alfuso, C. Polese, A. Liedl, GDI spray structure analysis by polycapillary X-ray -tomography, Int. J. Multiphas. Flow 70 (C) (2015) 15–21.

[44] A. Kastengren, C. F. Powell, Synchrotron X-ray techniques for fluid dynamics, Exp. Fluids 55 (3) (2014) 1686.

[45] A. L. Kastengren, F. Tilocco, D. Duke, C. Powell, X. Zhang, S. Moon, Time-Resolved X-Ray Radiography of Sprays from Engine Combustion Network Spray A Diesel Injectors, Atom. Sprays 24 (3) (2014) 251–272.

[46] J. P. Viera, R. Payri, A. B. Swantek, D. J. Duke, N. Sovis, A. L. Kastengren, C. F. Powell, Linking instantaneous rate of injection to X-ray needle lift measurements for a direct-acting piezoelectric injector, Energy Conversion and Management 112 (2016) 350–358. doi:10.1016/j.enconman.2016.01.038.

[47] A. B. Swantek, A. L. Kastengren, D. J. Duke, F. Z. Tilocco, N. Sovis, C. Powell, Quantification of Shot-to-Shot Variation in Single Hole Diesel Injectors, SAE Int. J. Fuels Lubr. 8 (1) (2015) 160–166.

[48] D. J. Duke, A. B. Swantek, N. Sovis, Z. Tilocco, C. F. Powell, Time-resolved x-ray tomography of gasoline direct injection sprays, SAE Paper (2015) 2015–01–1873.

[49] T. Li, S. Moon, K. Sato, H. Yokohata, A comprehensive study on the factors affecting near-nozzle spray dynamics of multi-hole GDI injectors, Fuel (2016) 1–11.

[50] Sandia National Laboratories, Engine Combustion Network "Spray G" Operating Condition, accessed Oct. 20, 2015 (2015).
URL http://www.sandia.gov/ecn/G/targetCondition/sprayG.php

[51] A. L. Kastengren, F. Z. Tilocco, C. Powell, J. Manin, L. M. Pickett, R. Payri, T. Bazyn, Engine Combustion Network (ECN): Measurements of Nozzle Geometry and Hydraulic Behavior, Atom. Sprays 22 (12) (2012) 1011–1052.

[52] M. L. Glodowski, D. J. Michalek, L. W. Evers, The Use of Results from Computational Fluid Dynamic Fuel Injector Modeling to Predict Spray Characteristics, in: F & L, SAE International, 1996, p. 961191.

[53] T. Luccini, G. D'Errico, N. Nordin, CFD Modelling of Gasoline Sprays, SAE Technical Paper 2005-24-086.

[54] B. Befrui, G. Corbinelli, M. D'Onofrio, D. Varble, GDI Multi-Hole Injector Internal Flow and Spray Analysis, SAE Technical Paper 2011-01-1211.

[55] K. Saha, S. Som, M. Battistoni, Y. Li, S. Quan, P. K. Senecal, Modeling of internal and near-nozzle flow for a gdi fuel injector, in: Proc ICEF2015, Houston, TX USA, 2015.

[56] M. Moulai, R. Grover, S. Parrish, D. Schmidt, Internal and Near-Nozzle Flow in a Multi-Hole Gasoline Injector Under Flashing and Non-Flashing Conditions, SAE Technical Paper 2015–01–0944.

[57] D. J. Duke, D. P. Schmidt, K. Neroorkar, A. L. Kastengren, C. Powell, High-resolution large eddy simulations of cavitating gasoline-ethanol blends, Int. J. Engine Res. 14 (6) (2013) 578–589.

[58] E. T. Baldwin, R. O. Grover Jr, S. E. Parrish, D. J. Duke, K. E. Matusik, C. Powell, A. L. Kastengren, D. P. Schmidt, String Flash-Boiling in Gasoline Direct Injection Simulations with Transient Needle Motion, Int. J. Multiphas. Flow 87 (2016) 90–101.

[59] R. Payri, J.Gimeno, P. Marti-Aldaravi, D.Vaquerizo, Internal Flow Characterization on an ECN GDi Injector, Atomization & Sprays 26 (9) (2016) 889–919.

[60] D. L. S. Hung, D. L. Harrington, A. H. Gandhi, L. E. Markle, S. E. Parrish, J. S. Shakal, H. Sayar, S. D. Cummings, J. L. Kramer, Gasoline Fuel Injector Spray Measurement and Characterization - A New SAE J2715 Recommended Practice, SAE Int. J. Fuels Lubr. 1 (1) (2008) 534–548.

[61] A. Kastengren, C. F. Powell, D. Arms, E. M. Dufresne, H. Gibson, J. Wang, The 7BM beamline at the APS: a facility for time-resolved fluid dynamics measurements, J. Synchrotron Rad. 19 (4) (2012) 654–657.

[62] D. Gursoy, F. De Carlo, X. Xiao, C. Jacobsen, TomoPy: a framework for the analysis of synchrotron tomographic data, J. Synchrotron Rad. 21 (2014) 1188–1193.

[63] K. Matusik, D. Duke, C. Powell, A. Kastengren, High resolution x-ray tomography of injection nozzles, in: Proc. 28th American Conference on Liquid Atomization and Spray Systems (ILASS-Americas), Dearborn, Michigan, 2016.

[64] J. Duran, B. Coll, C. Sbert, Chambolle's projection algorithm for total variation denoising, Image Processing On Line 3 (2013) 311–331. doi:10.5201/ipol.2013.61.

[65] T. Fogal, J. Krüger, Tuvok, an Architecture for Large Scale Volume Rendering, in: Proceedings of the 15th International Workshop on Vision, Modeling, and Visualization, Siegen, Germany, 2010.
URL http://www.sci.utah.edu/~tfogal/academic/tuvok/Fogal-Tuvok.pdf

[66] D. J. Duke, C. E. A. Finney, A. Kastengren, K. Matusik, N. Sovis, L. Santodonato, H. Bilheux, D. Schmidt, C. Powell, T. Toops, High-Resolution X-Ray and Neutron Computed Tomography of an Engine Combustion Network Spray G Gasoline Injector, SAE Int J Fuels & Lubricants 10 (2).

[67] D. J. Duke, A. Swantek, A. Kastengren, K. Fezzaa, C. Powell, Recent Developments in X-ray Diagnostics for Cavitation, SAE Int. J. Fuels Lubr. 8 (1) (2015) 135–146.

[68] Q. Shen, W.-K. Lee, K. Fezzaa, Y. S. Chu, F. De Carlo, P. Jemian, J. Ilavsky, M. Erdmann, G. G. Long, Dedicated full-field X-ray imaging beamline at Advanced Photon Source, Nucl. Instr. Meth. Phys. Res. A 582 (1) (2007) 77–79.

[69] D. J. Duke, A. Swantek, Z. Tilocco, A. Kastengren, K. Fezzaa, K. Neroorkar, M. Moulai, C. Powell, D. Schmidt, X-ray Imaging of Cavitation in Diesel Injectors, SAE Int. J. Engines 7 (2) (2014) 1003–1016.

[70] J. Manin, A. Kastengren, R. Payri, Understanding the Acoustic Oscillations Observed in the Injection Rate of a Common-Rail DI Diesel Injector, in: Proc. ASME 2012 Internal Combustion Engine Division Spring Technical Conference, 2012, pp. 379–391. doi:10.1115/ICES2012-81223.

[71] S. Moon, K. Komada, K. Sato, H. Yokohata, Y. Wada, N. Yasuda, Ultrafast X-ray study of multi-hole GDI injector sprays: Effects of nozzle hole length and number on initial spray formation, Exp. Therm. Fluid Sci. 68 (C) (2015) 68–81.

[72] D. J. Duke, A. B. Swantek, N. Sovis, F. Z. Tilocco, D. Gürsoy, T. Biçer, A. L. Kastengren, C. F. Powell, Time-resolved x-ray tomography of gasoline direct injection sprays, SAE Technical Paper 2015-01-1873.

[73] Z. Wang, A. B. Swantek, R. Scarcelli, D. J. Duke, A. L. Kastengren, C. Powell, S. Som, LES of Diesel and Gasoline Sprays with Validation against X-Ray Radiography Data, SAE Int. J. Fuels Lubr. 8 (1) (2015) 147–159.

[74] A. L. Kastengren, C. Powell, Y. Wang, K. S. Im, J. Wang, X-Ray Radiography Measurements of Diesel Spray Structure at Engine-Like Ambient Density, in: Proceedings of the ILASS-Americas 21st Annual Conference on Liquid Atomization and Spray Systems, Orlando, FL, 2008.

[75] W. M. Pitts, Effects of global density ratio on the centerline mixing behavior of axisymmetric turbulent jets, Exp. Fluids 11 (2-3) (1991) 125–134.

[76] D. Siebers, Scaling Liquid-Phase Fuel Penetration in Diesel Sprays Based on Mixing-Limited Vaporization, SAE Technical Paper 1999-01-0528. doi:10.4271/1999-01-0528.

[77] D. J. Duke, A. B. Swantek, A. L. Kastengren, D. Gursoy, T. Bicer, C. F. Powell, Video media: X-ray tomography of multi-hole gasoline direct injectors, accessed Feb. 29, 2016 (2016).
URL https://youtu.be/4WNICOpPpGU

[78] P. Strek, D. J. Duke, A. Swantek, A. L. Kastengren, C. Powell, X-Ray Radiography and CFD Studies of the Spray G Injector, SAE Technical Paper (2016) 2016–01–0858.

[79] K. Saha, S. Som, M. Battistoni, Y. Li, S. Quan, P. K. Senecal, Numerical simulation of internal and near-nozzle flow of a gasoline direct injection fuel injector, J. Phys. Conf. Ser. 656 (2015) 012100–5.

[80] K. Saha, S. Som, M. Battistoni, Y. Li, E. Pomraning, P. K. Senecal, Numerical Investigation of Two-Phase Flow Evolution of In- and Near-Nozzle Regions of a Gasoline Direct Injection Engine During Needle Transients, SAE Int. J. Engines 9 (2) (2016) 1230–1240.

[81] L. Itani, G. Bruneaux, L. Hermant, C. Shulz, Investigation of the mixing process and the fuel mass concentration fields for a gasoline direct-injection spray at ECN Spray G conditions and variants, JSAE/SAE Paper 2015-09-01. doi:10.4271/2015-01-1902.

Duke, D.J., Kastengren, A.L., Matusik, K.E., Swantek, A.B., Powell, C.F., Payri, R., Vaquerizo, D., Itani, L., Bruneaux, G., Grover, R.O., Parrish, S., Markle, L., Schmidt, D., Manin, J., Skeen, S.A., Pickett, L.M., 2017. Internal and near nozzle measurements of Engine Combustion Network "Spray G" gasoline direct injectors. Exp. Therm. Fluid Sci. 88, 608–621. doi:10.1016/j.expthermflusci.2017.07.015